Intrinsic kinetics of steam methane reforming on a thin, nanostructured and adherent Ni coating

Florent Minette[a], Michael Lugo-Pimentel[b], Dean Modroukas[c], Andrew W. Davis[d], Rajinder Gill[d], Marco J. Castaldi[b], Juray De Wilde[a],*

[a] Université catholique de Louvain, Materials & Process Engineering (IMAP), Place Sainte Barbe 2, B-1348 Louvain-la-Neuve, Belgium
[b] City University of New York, City College, Dept. of Chemical Engineering, New York, NY, USA
[c] Innoveering LLC, Ronkonkoma, NY, USA
[d] Alloy Surfaces, Co. Inc. (ASC), Chester Township, PA, USA

ARTICLE INFO

ABSTRACT

The intrinsic kinetics of Steam Methane Reforming (SMR) on a non-conventional nanostructured and strongly adherent Ni coating on a metal substrate was experimentally studied using an integral packed bed reactor. The coating was characterized by means of SEM, N_2 adsorption/desorption, EDX, XRD and TPR. The reactor was designed and the operating conditions selected to guarantee negligible interfacial and intra-particle transport limitations, plug flow, isothermal operation and a sufficiently small pressure drop. Experiments were carried out at temperatures between 450 and 600 °C, space times between 0.033 and 0.1 mol/(g_{cat}.s) and steam-to-carbon ratios of 2.87 to 5.53. Discrimination between potential reaction mechanisms and rate determining steps and estimation of the rate parameters and their confidence intervals followed from regression and statistical and physicochemical testing. Measurements confirmed that the water gas shift reaction reached equilibrium for each condition. A comparison with reported intrinsic kinetics for a conventional SMR catalyst was made and optimal catalyst coating thickness, accounting for intra-catalyst diffusion limitations was evaluated.

1. Introduction

Hydrogen is expected to play an increasingly important role in the refining and petrochemical industries, but also as future energy carrier [1]. Although significant progress has been made towards efficient electrochemical and photocatalytic production of hydrogen [2–8], the widely used conversion of natural gas to hydrogen/syngas by steam methane reforming (SMR) is expected to play a crucial role in the successful transition to a hydrogen economy. The conversion of natural gas to clean synthetic fuels [9–14] and combined steam and dry reforming [15–20] also gained interest, driven by the availability of natural gas and concerns about CO_2 emissions-related global warming [21–23]. The increase in hydrogen demand is expected to be further fueled by the growing fertilizer market and related ammonia production [24]. Increasing the capacity and efficiency of steam methane reformers therefore recently gained attention from the industries but faces limitations related to the currently used reactor technology.

Steam methane reforming is conventionally done in multi-tubular packed bed reactors using $Ni/MgAl_2O_4$ catalyst pellets. To supply the heat for the strongly endothermic reactions, the reactor tubes are suspended in a furnace. Heat transfer between the tube inner wall and the process gas is often limiting the reactor performance. Radial temperature uniformity is maintained by using 4 inch-diameter tubes. To limit the pressure drop in the 11–12 m long packed beds, relatively large cm-sized pellets are used, introducing strong intra-particle diffusion limitations. A catalytically active layer of a couple of millimeters therefore is utilized with the particles being perforated to reduce the diffusion distance and increase the amount of active catalyst layer. Despite that, catalyst effectiveness factors for the steam reforming reactions are typically low, of the order of 2–5% [25].

Structured catalytic reactors can manage many of the limitations introduced by conventional catalyst pellets. For example, a structured metal substrate with a thin Ni coating (typically a few microns) can be used. Whereas the use of a thin catalyst layer allows operating with high catalyst effectiveness factors, the metal substrate itself can be structured to minimize the pressure drop and intensify the heat transfer between the tube inner wall and the process gas. The "bed density", which can be calculated from the specific geometric surface area (m^2 catalyst interface per m^3 reactor) and the catalyst layer thickness, is typically lower than that of conventional packed beds, but this can be

---

* Corresponding author.
  E-mail address: juray.dewilde@uclouvain.be (J. De Wilde).

Nomenclature

$A(k_i)$	Preexponential factor of rate coefficient ki
$A(K_A)$	Preexponential factor of adsorption constant KA
$a_{v,s}$	the specific external particle surface, per unit volume particle [m² interface/m³ solid] (solid includes inert and catalyst particles)
Bi_w	the thermal Biot number at the inner wall, $Bi_w = h_{iw} \cdot d_p / \lambda_{er}$ [/]
b	the volumetric bed dilution [m³ inert/m³ solid]
b_{max}	the maximum volumetric bed dilution [m³ inert/m³ solid]
C_A	the concentration of A in the bulk fluid [kmol A/m³ fluid]
$(C_{A,s})^s$	the concentration of A in the fluid at the external surface of the solid [kmol A/m³ fluid]
$\Delta C_{A,gs}$	the difference between the concentration of A in the bulk fluid and at the particle surface [kmol A/m³ fluid]
C_0	the total molar concentration at the inlet [kmol/m³ fluid]
$c_{P,g}$	the gas phase heat capacity [kJ/(kg gas·K)]
D_g	or D_{Am} the diffusivity of the gas phase / of A in the gas mixture [m² gas/s] or [m² catalyst/s]
$D_{A,eff}$	$= D_{Am} \cdot \varepsilon_s / \tau$ the effective diffusivity of A in the catalyst [m³ fluid/(m catalyst·s)]
D_{ea}	the axial dispersion coefficient [m² reactor/s]
D_{kA}	Knudsen diffusivity [m³ fluid/(m catalyst.s)]
d_p	the particle diameter [m]
d_t	the inner tube or bed diameter [m reactor]
E_a	the activation energy of the reaction [kJ/kmol]
f	the friction factor [/]
G	the fluid mass flux [kg fluid/(m² reactor·s)]
$(-\Delta H_i)$	the heat of reaction [kJ/kmol]
$(-\Delta H_A)$	adsorption enthalpy of specie A [kJ/kmol]
h	catalytic layer thickness [m]
h_{gs}	the gas-solid heat transfer coefficient [kJ/(m² interface·s·K)]
h_{iw}	the heat transfer coefficient at the inner wall [kJ/(m² interface·s·K)]
$j_{D/H}$	$= f(Re_p)$ the j-factor for mass/heat transfer [/]
k_1	rate coefficient of reactions I [mol. bar$^{1/2}$/(kg$_{cat}$.s)]
k_2	rate coefficient of reaction II [mol/(kg$_{cat}$.s.bar)]
k_3	rate coefficient of reactions III [mol. bar$^{1/2}$/(kg$_{cat}$.s) for model A and mol /(kg$_{cat}$.s) for model B]
k_g	the gas-solid mass transfer coefficient [m³ fluid/(m² interface·s)]
L	the bed length [m]
M_m	the fluid molecular mass [kg/kmol]
n	the reaction order [/]
p_A	the partial pressure of specie A [bar]
P_{tot}	the total pressure [bar]
ΔP	the pressure drop [bar]
Pe_{ma}	$= u_{sup} \cdot d_p / (\varepsilon \cdot D_{ea})$ the Péclet number for axial mass transport [/] (typical values between 1 and 2)
Pe_{mr}	$= u_{sup} \cdot d_p / (\varepsilon \cdot D_{er})$ the Péclet number for radial mass transport [/] (typical values between 8 and 12)
Pr	$= \mu_g \cdot c_{P,g} / \lambda_g$ the Prandtl number [/]
R	the universal gas constant [kJ/(kmol K)]
Re_p	$= \rho_g \cdot u_{sup} \cdot d_p / \mu_g = G \cdot d_p / \mu_g$ the particle Reynolds number [/]
$RI_{im,r}$	the maximum allowable relative importance of interfacial mass transfer limitations for a given reaction rate [%]
r_A	the intrinsic reaction rate of A [mol A/(kg catalyst·s)]
r_{A0}	the reaction rate of A at the reactor inlet [mol A/(kg catalyst·s)]
r_i	the intrinsic rate of reaction i [mol/(kg catalyst·s)]
$\tilde{r}_i$	the observed rate of reaction i [mol/(kg catalyst·s)]
r_p	pore radius [m]
Δr_{rel}	the maximum acceptable relative difference between the observed and intrinsic reaction rates [%]
ΔS_A	adsorption enthalpy of specie A [kJ/(mol.K)]
Sc	$= \mu_g / (\rho_g \cdot D_g)$ the Schmidt number [/]
T	the bulk fluid temperature [K]
T_w	the inner reactor wall temperature [K]
ΔT_{ad}	the adiabatic temperature rise in the reactor [K]
$\Delta T_{int,s}$	the difference between the average particle temperature and the temperature at the external surface of the particle [K]
ΔT_{gs}	the difference between the bulk fluid and solid phase temperature [K]
$\Delta T_{r,B}$	the difference between the near-wall bed temperature and the average bed temperature [K]
$\Delta T_{w,Bc}$	the difference between the inner wall temperature and the centerline bed temperature [K]
u_{sup}	the superficial velocity [m³ fluid/(m² reactor·s)]
W	weight of catalyst [kg]
x_A	the conversion of A [/]
x_{dil}	the conversion obtained with the diluted bed
Δx_{rel}	the acceptable relative deviation of the conversion [%]
$(y_A)°$	the mole fraction of A in the feed [kmol A/kmol total]
y_f	the film factor [/]
ε	the bed porosity [m³ fluid/m³ reactor]
ε_s	the internal void fraction or porosity of the catalyst [m³ fluid/m³ catalyst]
η_i	catalyst effectiveness factor for reaction i
λ_{er}	the effective radial thermal conductivity of the bed [kW/(m reactor·K)]
λ_g	the gas phase thermal conductivity [kW/(m gas·K)]
λ_s	the solid phase thermal conductivity [kW/(m solid·K)]
ρ_B	the active bed density $= (1-\varepsilon) \cdot \rho_s \cdot (1-b)$ [kg catalyst/m³ reactor]
ρ_s	the active solid density [kg catalyst/m³ catalyst]
τ	the catalyst tortuosity [/]
ξ	non-dimensional position in the catalytic layer

compensated by the significantly higher catalyst effectiveness factors. Several structured catalytic reactor designs have been considered for use in steam methane reforming, such as ZoneFlow™ Reactor Technology [26]. Pressure drop and heat transfer have been characterized both experimentally and through detailed CFD (Computational Fluid Dynamics) simulations. If the intrinsic reaction kinetics for the catalyst used are known, CFD can also be used to calculate the reactor performance under typical commercial conditions and to study scale-up and optimization [27,28].

A critical issue in the conception of structured catalytic reactors is the deposition of a stable, well-anchored and active catalyst layer. A popular technique is wash-coating with a slurry containing the active catalyst [29–33]. While wash-coating is extensively used for pellets, with alternative substrate geometries (mesh, monolith, complex structures, etc.) it becomes challenging to ensure reproducibility, stability and minimal loss of catalyst (i.e. delamination) under severe operating conditions. To prevent the latter, pretreatment of the substrate is critical [34] but does not guarantee robust performance. Alternative techniques were proposed, based on the deposition of an intermediate structured ceramic layer (alumina) which acts as an anchor for the catalyst that is deposited by classical wash-coating. The presence of this intermediate layer was shown to increase the coating adherence [35–37] but can impact reaction performance. Solution combustion synthesis (SCS) followed by wet impregnation [38], physical vapor

deposition (PVD) [39], electrophoretic deposition [40] or chemical vapor deposition (CVD) [41] were also studied and show promise but are demanding processes for large scale operations.

In the present work, the intrinsic kinetics of steam methane reforming on a specific thin, nanostructured and adherent Ni coating is experimentally studied. This unconventional catalyst formulation process meets many of the challenges required for harsh environment performance and adds a new feature to catalyst design, the post-coating forming of the material to the final geometrical structure. Details on the catalyst and the experimental set-up are given in the next sections. The experimental results and kinetic modelling are discussed thereafter. Finally, an evaluation of the required coating thickness is made.

2. The ASC Ni catalyst

Alloy Surfaces Company, Inc. (ASC) has developed proprietary processing technology for producing thin, nanostructured Ni coatings on metal substrates. The coatings are interdiffused into the metallic foil substrate in-situ, resulting in strong adherence [42]. In a typical coating process, a metal substrate (Inconel) is coated with a slurry consisting of ASC's proprietary catalyst formulation using continuous web-based processes that allow precise control of coating thickness and uniformity. The coated metal substrate is then subjected to heat treatment under reducing environment resulting in the formation of various aluminides. This alloyed layer is bound to the metal substrate through metallically bonded inter-diffusion zones. The alloyed layer is then chemically treated to create the desired porosity, consequently resulting in a catalytically active surface. The inter-diffusion layer enables intimate connectivity between the active elements for reaction and the base substrate, resulting in mechanical robustness. These metal-supported catalyst materials (total thickness: 100–250 μm) provide unique advantages for hydrogen production via SMR at high space velocities, at least partly due to their ease of fabrication into complex geometries. Such geometries can be formed after deposition of the coating, in contrast to classical wash-coatings that have to be deposited after forming the structure.

The catalyst was characterized by SEM, EDX, XRD, TPR and nitrogen adsorption/desorption. SEM, EDX and XRD were performed on the catalyst material used for the kinetic testing, but in oxidized state. TPR and nitrogen adsorption/desorption used coating scraped off from the catalyst material. Fig. 1 shows an SEM picture of a cross section of the catalyst, which was previously embedded in an epoxy resin, and a picture of the external surface of the catalyst. Three layers are clearly visible in Fig. 1(a). The central substrate support is non-porous and inactive. The second layer is the uniform inner coating and is approximately 7 μm thick. The third layer (discontinuous due to epoxy) is the outer coating and averages 40 μm in this case, but can be varied.

The external surface uniformity of the coating can be seen in Fig. 1(b). Because of inter-diffusion, both the inner and external layers contain aluminum and nickel, as confirmed by energy-dispersive X-ray spectroscopy analysis, and are catalytically active. The EDX spectra for the intermediate and external layers are presented in Fig. 2(a–b). The presence of oxygen in the EDX spectra indicates catalyst in oxidized state. The XRD pattern of the catalyst in Fig. 2(c) shows, on the other hand, the characteristic peaks of Ni, observed at $2\theta = 44.2°$, $51.4°$ and $75.6°$. In contrast to what was observed by EDX, no peaks for NiO were observed, indicating the formation of a very thin NiO passivation layer upon contact with air. This explains the experimentally observed short catalyst reduction time.

Temperature Programmed Reduction (TPR) using scraped off coating confirmed the formation of a NiO passivation layer. Prior to the TPR tests, 350 mg of catalyst were placed in a quartz reactor and flushed with air at 200 °C for 2.0 h and then cooled to room temperature under N_2 flow. During the test, the temperature was increased from 50 °C to 600 °C under a 50% H_2/N_2 gas mixture flow at 40 ml/min, imposing a 10 °C/min heating rate. The consumption of H_2 was monitored via on-line mass spectrometer (QGA Hiden Analytical). The TPR profile is shown in Fig. 2(d). The main reduction peak around 300 °C is attributed to the reduction of NiO particles in low interaction with the support or the passivation layer over the exposed nickel. The broader consumption peak beginning at 425 °C and reaching a broad maximum near 475 °C and continuing until the termination of the test is attributed a strong NiO-support interaction [43,44]. Both of these consumption peaks are consistent with the ASC formulation having both the outer and inner coatings respectively.

The pore size distribution and surface area of a used catalyst coating were measured by nitrogen adsorption and desorption in a TriStar 3000 gas adsorption analyser. A total of 476 mg of intermediate and external layer, separated from the Inconel support, was used for the analysis. Vacuum degassing was carried out at 300 °C during 12 h. The temperature was then reduced to 77.15 K and the pressure was incrementally increased for adsorption and then decreased for desorption. The recorded volume of adsorbed gas was correlated to the pore size distribution and the total surface area, using the standard BET analysis. The cumulative and incremental pore size profiles are shown in Fig. 3. The porosity was measured to be 0.084 and the BET surface area 7.4 m^2/g, relatively low but consistent with the methodology used to produce the catalyst [42]. Direct comparison with conventional Ni-based SMR catalysts is difficult, with large variations on the reported values. Ross and Steel (1973) and Sepehri et al. (2016) reported BET surface areas above 150 m^2/g for conventional fresh Ni/Al_2O_3 catalyst [45,46], whereas Hou and Hugues (2001) and Yang (2017) reported respectively 14.3 and 26.3 m^2/g for tested catalyst [47,48]. Xu and Froment (1989) studied a $Ni/MgAl_2O_4$ catalyst and reported a BET
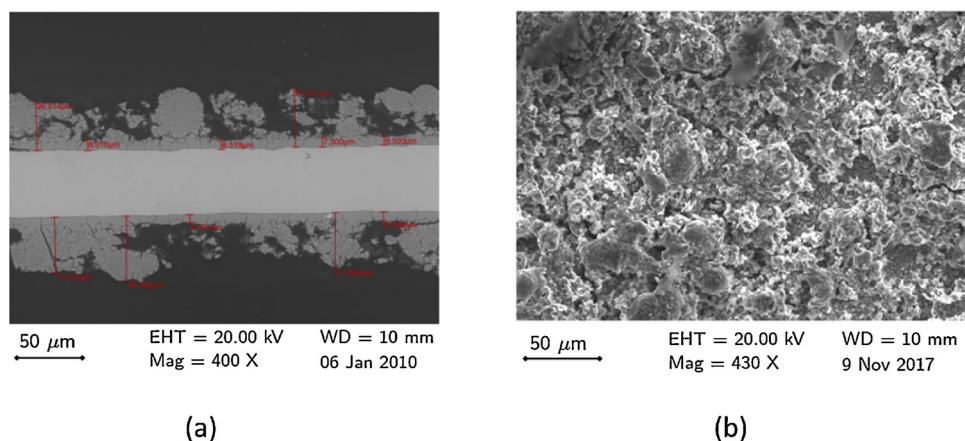

Fig. 1. SEM picture of (a) a cross section and (b) the external surface of the ASC catalyst.
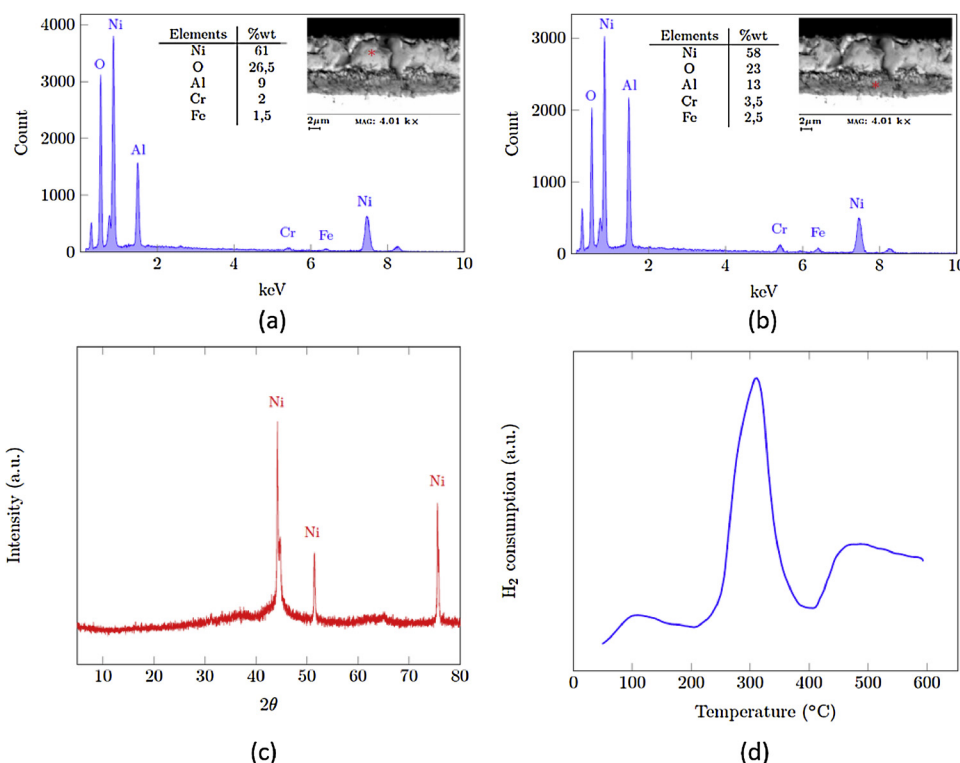
Fig. 2. EDX spectra of the (a) intermediate and (b) external layers of an oxidized sample of the ASC catalyst with the chemical composition in mass fraction, (c) XRD pattern and (d) TPR profile of the catalyst.
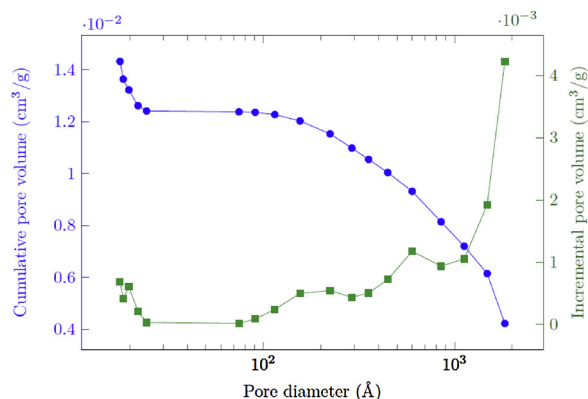

Fig. 3. Cumulative and incremental pore volume versus the pore diameter for the intermediate and external layers (oxidized sample).

surface area of $58\,\mathrm{m^2/g}$ for fresh catalyst [49]. A wide range of reported BET surface areas is also reported for structured catalysts. Liu et al. (2012) measured a BET surface area of $174\,\mathrm{m^2/g}$ for a fresh Ni catalyst used in micro-channel reactors [36], while Vita et al. (2015) obtained $5.3\,\mathrm{m^2/g}$ for a Ni/CeO_2 coating over a cordierite monolith [38].

Table 1 summarizes the main physical properties of the intermediate and external layers of the ASC coating in oxidized state.

3. Experimental set-up

The experiments were carried out in a tubular fixed bed reactor in integral operation. A simplified schematics of the experimental setup is shown in Fig. 4. Detailed information can be found in Lugo-Pimentel (2017) [50]. All gases (N_2, CH_4 and H_2 - T.W. Smith, Research Grade, 5.0) were introduced to the reactor via mass flow controllers (Tylan FC-280S) (3) and pre-heated via a resistive heat tape (Omega Engineering, cat #SST051-080) wrapped around a ¼" stainless steel tube controlled

by a Variac regulator (6). Water was introduced via a vaporizer system (5). Distilled water was fed from a pressurized cylinder using a regulation valve to ensure a uniform delivery pressure. The water passed through a $10\,\mu m$ filter (Swagelok SS-4MG) followed by a high-precision metering valve and a downstream rotameter (4) (Gilmont instruments GF2060) and was evaporated prior to mixing with the other gases in a mixing chamber (7). The gas flow controllers had an accuracy of ± 1% of full scale, whereas the water flow controller had an accuracy of ± 5% of the reading. The pre-heated gas mixture is fed to the reactor (1) installed in a 5-zone vertical electric furnace (Mellon Company) (2) controlled to achieve the target reactor temperature. Immediately after exiting the reactor, the product mixture is cooled in an ice bath to condense water (8). The pressure in the reactor is set using a metering valve (Swagelok SS-4L-MH). The dry effluent is directed to a micro-gas chromatograph (Inficon series 3000) quantifying CH_4, CO_2, CO, H_2, N_2 with provisions to identify C_2 species. Mass balances determined primarily using carbon were closed within 5% or less and confirmed using hydrogen and oxygen balances.

Prior to kinetic testing, the reactor was always purged and the catalyst conditioned with a 17% H_2/N_2 mixture while the target temperature of 600 °C was achieved at a rate of 20 °C min^{-1}. The reactor was kept at 600 °C for 1.5 h to ensure a consistent catalyst surface baseline. Xu and Froment [49] observed a rapid decrease in activity during the first 24 h a conventional Ni catalyst was on stream. The data

Table 1

ASC coating physical properties (intermediate + external layers, oxidized state).

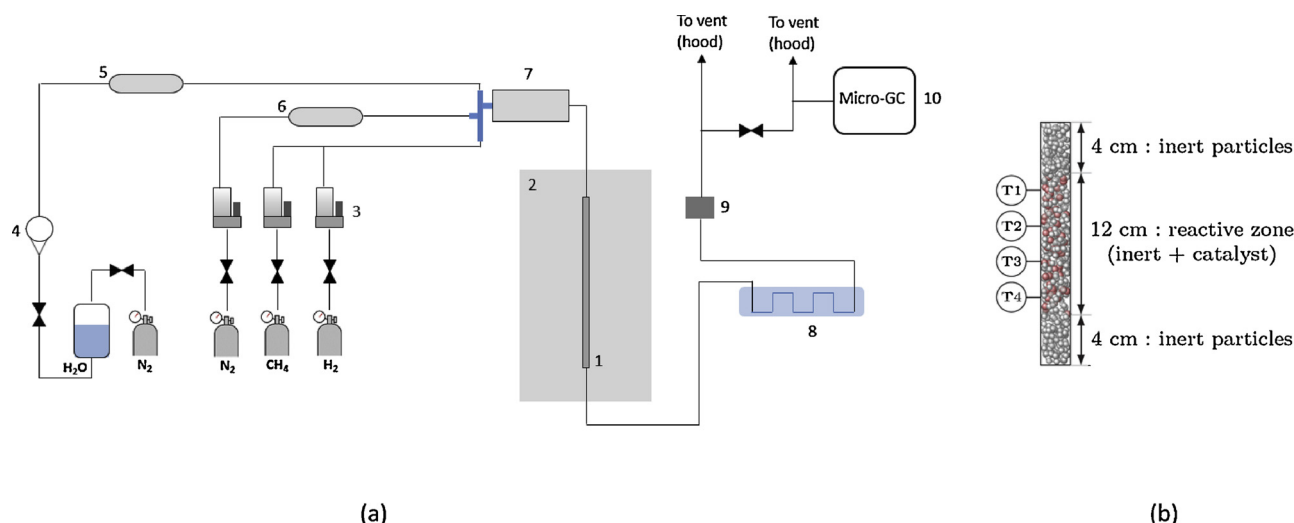|	
Coating thickness (μm)	7 + 40(Fig.1-a)
Coating mass fraction (g_{coat}/g_{tot})	0.075
Ni content (wt.%) (reduced state)	75-85
BET surface area (m^2/g_{coat})	7.4
Density (g_{coat}/cm^3_{coat})	5.78
Pore volume (cm^3_{coat}/g_{coat})	0.0145
Porosity (cm^3_g/cm^3_{coat})	0.084

Fig. 4. (a) Flowsheet of the experimental setup: 1: tubular fixed bed reactor, 2: furnace, 3: mass flow controllers, 4: rotameter, 5: evaporator, 6: pre-heater, 7: mixing chamber, 8: ice water bath, 9: water trap, 10: gas chromatograph. (b) Details of the micro-packed bed reactor.

that were used for the kinetic modelling in this study were obtained with a catalyst that had been more than 50 h on stream.

4. Experimental reactor design and operating conditions

The reactor was designed and the window of operating conditions determined to allow studying the intrinsic reaction kinetics. Several constraints have to be met that are not easily combined. Verifying the functional form of a rate expression is in practice only possible on the basis of isothermal data [51]. This implies that radial and axial temperature gradients in the reactor have to be kept sufficiently small. An ideal plug flow type flow pattern is aimed at to facilitate the interpretation and treatment of the data. Furthermore, interfacial mass and heat transfer limitations and intra-particle diffusion limitations have to be avoided. Finally, a sufficiently low pressure drop across the bed is required. Criteria discussed hereafter have been developed to evaluate the above constraints and have been used to design the reactor and select the experimental operating conditions. The main reactor design

parameters are the bed diameter and length and the particle diameter and bed dilution. The experimental conditions include the different feed flow rates and the operating pressure and temperature. Application of certain criteria requires known reaction kinetics. Because the kinetics with the ASC catalyst is not a priori known, the criteria are first evaluated using the Xu and Froment (1989) kinetics for a conventional Ni catalyst [49]. After deriving the kinetics for the ASC catalyst from the experimental data, it was re-verified that for all the experimental conditions listed in Table 4, the criteria of Table 2 were respected.

To guarantee plug flow, the velocity has to be sufficiently high such that $Re_p = G \cdot d_p / \mu_g > 10\text{--}20$ [52]. For a negligible effect of axial dispersion, the bed has to be sufficiently long compared to the particle diameter. Carberry and Wendel (1963) found $L/d_p > 20\text{--}50$ is required [53]. Young and Finlayson (1973) proposed a criterion based on the comparison of the reaction and axial dispersion time scales, i.e. $Pe_{ma} = u_{sup} \cdot d_p / (\varepsilon \cdot D_{ea}) > > r_{A0} \cdot \rho_B \cdot d_p / (u_{sup} \cdot C_0)$ with typical values of Pe_{ma} between 1 and 2 [54]. The criteria involving the reaction kinetics are usually evaluated at the reactor inlet where the reaction rates are

Table 2
Criteria for the design of a lab-scale fixed bed reactor and the selection of the operating conditions to study intrinsic reaction kinetics.

Plug flow	$Re_p = \frac{G d_p}{\mu_g} > 10\text{--}20$	Carberry, 1976 [52]
Negligible axial dispersion	$\frac{L}{d_p} > 20\text{--}50$	Carberry and Wendel, 1963 [53]
	$Pe_{ma} = \frac{u_s d_p}{\varepsilon D_{eA}} \gg \frac{r_{A0} \rho_b d_p}{u_s C_0}$	Young and Finlayson, 1973 [54]
Negligible radial dispersion	$\frac{d_t}{d_p} > 8\text{--}10$	Chu and Ng, 1989 [55]
Radial temperature difference	If $d_t/d_p > 100$:	
	$\Delta T_{r,B} = \|-\Delta H\| \, r_A \rho_b \frac{(d_t)^2}{32 \lambda_{er}} < \Delta r_{rel} \frac{R T_w^2}{E_a}$	Mears, 1971 [56,57]
	If $d_t/d_p < 100$:	
	$\Delta T_{w,Bc} = (1 + 8 \frac{d_p}{Bi_w d_t}) \|-\Delta H\| \, r_A \rho_b \frac{(d_t)^2}{32 \lambda_{er}} < \Delta r_{rel} \frac{R T_w^2}{E_a}$	
Maximum volumetric bed dilution	$b_{max} = \frac{\Delta x_{rel}}{\Delta x_{rel} + 0.5 x_{dil} \frac{d_p}{L}}$	Berger, 2002 [59,60,61]
Gas-catalyst heat transfer limitations	$\Delta T_{gs} = \frac{\|-\Delta H\| \, r_A \rho_b d_p}{6 h_{gs}} < \Delta r_{rel} \frac{R T^2}{E_a}$	Mears, 1971 [56,57]
Gas-catalyst mass transfer limitations	$\Delta C_{gs} = \frac{r_A \rho_s}{k_{gs} a_{vs}} < \Delta r_{rel} \frac{C_A}{n}$	Mears, 1971 [56,57]
Negligible intra-catalyst diffusion limitations	$\Phi = \left(\frac{n+1}{2}\right)\left(\frac{r_A \rho_s}{D_{A,eff} C_{As}^s a_{vs}^2}\right)$	Weisz and Prater, 1954 [63]
Negligible intra-catalyst heat transfer limitations	$\Delta T_{int,s} = \frac{\|-\Delta H\| \, r_A \rho_s d_p^2}{60 \lambda_s} < \Delta r_{rel} \frac{R T^2}{E_a}$	Anderson, 1963 [64]
Small pressure drop	$\Delta P < 0.2 \frac{P_{tot}}{n}$	

assumed maximum under isothermal operation. A negligible effect of radial dispersion and avoiding short-circuiting along the wall requires a sufficiently high tube-to-particle diameter ratio, $d_t/d_p > 8$–10 [55]. Eventually $Pe_{mr} = u_{sup} \cdot d_p/(\varepsilon \cdot D_{er})$ can be calculated. For $10 < Re_p < 2000$, $Pe_{mr}/[1 + 19.4(d_p/d_t)^2]$ has a typical value between 8 and 12.

To avoid radial temperature and resulting concentration gradients and guarantee isothermal operation, the tube diameter, d_t, cannot be too large. Mears (1971) derived criteria for the maximum allowable radial temperature difference in the reactor for a maximum acceptable relative difference between the observed and intrinsic reaction rates, Δr_{rel} (in %, e.g. 0.05) [56,57]. For $d_t/d_p > 100$, $\Delta T_{r,B} = |-\Delta H| \cdot r_A \cdot \rho_B \cdot (d_t)^2/ (32 \cdot \lambda_{er}) < \Delta r_{rel} \cdot R \cdot (T_w)^2/E$, where $\Delta T_{r,B}$ is the difference between the near-wall bed temperature and the average bed temperature. For $d_t/d_p < 100$, $\Delta T_{w,Bc} = [1 + 8 \cdot d_p/(Bi_w \quad d_t)] \cdot |-\Delta H| \cdot r_A \cdot \rho_B \cdot (d_t)^2/ (32 \cdot \lambda_{er}) < \Delta r_{rel} \cdot R \cdot (T_w)^2/E$ where $\Delta T_{w,Bc}$ is the difference between the inner wall temperature and the centerline bed temperature and Bi_w the thermal Biot number at the inner wall, $Bi_w = h_{iw} \cdot d_p/\lambda_{er}$. The effective radial thermal conductivity of the bed, λ_{er}, and the heat transfer coefficient at the inner wall, h_{iw}, can be calculated as in De Wasch and Froment (1972) [58]. With highly exo- or endothermic reactions, such as steam methane reforming, the radial temperature difference in the reactor can only be kept sufficiently small by diluting the particle bed. Uniformity has to be guaranteed and excessive dilution avoided. Berger et al. (2002) derived a criterion for the maximum volumetric bed dilution, b_{max}, as a function of the acceptable relative deviation of the conversion, Δx_{rel}, in % (e.g. 0.05). It was shown that $b_{max} = \Delta x_{rel}/(\Delta x_{rel} + 0.5 \cdot x_{dil} \cdot d_p/L)$ with x_{dil} the conversion obtained with the diluted bed [59–61].

Negligible interfacial mass and heat transfer limitations require sufficient turbulence and operation at sufficiently high flow velocity, not evident in an experimental reactor [62]. For a gas phase reaction in a packed bed, Mears (1971) proposed a criterion to estimate the maximum allowable temperature difference between the process gas and the catalyst surface, ΔT_{gs}, based on a maximum acceptable relative difference between the observed and intrinsic reaction rates, Δr_{rel} (in %, e.g. 0.05). It was shown that $\Delta T_{gs} < \Delta r_{rel} \cdot R \cdot (T)^2/E$. The expected ΔT_{gs} can be estimated from $\Delta T_{gs} = |-\Delta H| \cdot r_A \cdot \rho_B \cdot d_p/(6 \cdot h_{gs})$. In a similar way, a criterion for the maximum allowable relative importance of interfacial mass transfer limitations for a given reaction rate, Δr_{rel} (in %, e.g. 0.05) was derived by Mears (1971). It was shown that $\Delta C_{A,gs} < \Delta r_{rel} \cdot C_A/n$, where $\Delta C_{A,gs}$ can be calculated from $r_A \cdot \rho_s/(k_g \cdot a_{v,s})$ and $a_{v,s}$ is the specific external surface area per unit volume particle [56,57]. Correlations for the gas-solid heat and mass transfer coefficients in packed beds, h_{gs} and k_g, can be found in Froment et al. (2010) [51]. The absence of interfacial transfer limitations can eventually be experimentally verified by varying the molar flow rate F at given space time W/F, where W is the mass of catalyst in the bed.

Weisz and Prater (1954) derived a criterion for negligible intraparticle diffusion limitations, later extended by different authors [63]. For an n-th order reaction, $\Phi = [(n+1)/2] \cdot [(r_A \cdot \rho_s)/ (D_{A,eff} (C_{A,s})^s \cdot (a_{v,s})^2)] << 1$. The concentration of A in the fluid at the catalyst surface can be estimated from $(C_{A,s})^s = C_A - \Delta C_{A,gs}$. For the verification of the Weisz-Prater criterion and considering excess steam, a first order steam methane reforming reaction was assumed. Experimentally, the absence of intra-particle diffusion limitations can be verified by reducing the dimensions of the catalyst particles until no effect on the measured reaction rates is observed. Intra-particle heat transfer resistance is typically negligible, but can be verified using Anderson's criterion [64], based on the maximum allowable difference between the average solid particle temperature and the temperature at the external surface of the particle for a maximum allowable relative difference between the observed and isothermal/intrinsic reaction rate, Δr_{rel} (in %, e.g. 0.05), i.e. $\Delta T_{int,s} < \Delta r_{rel} \cdot R \cdot (T)^2/E$. The actual $\Delta T_{int,s}$ can be estimated from $\Delta T_{int,s} = |-\Delta H| \cdot r_A \cdot \rho_s \cdot (d_p)^2/(60 \cdot \lambda_s)$. Finally, the pressure drop over the bed has to be kept sufficiently small. A frequently used criterion is $\Delta P < 0.2 \cdot P_{tot}/n$, with n the reaction order. The pressure drop over the bed, ΔP, can be calculated from the Ergun equation [65]. The different criteria are summarized in Table 2.

Meeting all criteria limits the window of operating conditions in which experiments can be carried out. The catalyst foil was perforated into small disks, 2.5 mm in diameter and 1.52 mm in equivalent diameter. Perforating smaller disks was not possible without significantly damaging the catalyst. Guaranteeing isothermal operation is challenging with the highly endothermic steam methane reforming reactions. Bed dilution was applied to reduce the specific heat consumption. The reactor was loaded with 1.5 g of catalyst mixed with 28.5 g of α-alumina diluent particles, 300 μm in diameter. Because of the strong bed dilution, the criteria for plug flow, axial and radial dispersion, radial temperature uniformity, interfacial mass and heat transfer limitations and pressure drop are evaluated using the diameter of the inert particles. The criteria for intra-catalyst diffusion and heat transfer are verified using the catalyst coating thickness. To further dampen the reaction rates in the inlet region and the heat consumption in general, hydrogen is co-fed at a H_2/C-ratio of 1.25 with the methane/steam-mixture in the steam methane reforming experiments. The reactor housing was manufactured from Inconel-625 with a 1.0 cm inner diameter. The total length is 20 cm, including a top and bottom inert bed, 4 cm long each, to have a 12 cm length active bed. Five k-type, 1.6 mm diameter thermocouples (Omega Engineering) were located equidistant along the length of the reactor providing center and radial measurements. The average temperature is reported and is measured with an error of ± 3 °C. In all tests, the temperature difference over the bed could be kept below 6 °C.

The operating conditions at which experiments were carried out are given in Table 3. Within the range of possible operating conditions, experiments were carried out at 5 different target temperatures (± 450, 510, 550, 570 and 600 °C). For each temperature, the space time was varied, keeping the S/C-ratio and the H_2/C-ratio at target values. At two temperatures, an additional experiment was carried out, changing the S/C-ratio. The temperature is lower than that practiced in commercial operation in order to avoid temperature gradients or reaching chemical equilibrium, that prevent measuring intrinsic reaction kinetics.

5. Kinetic modelling and parameter estimation

5.1. Reaction mechanism and kinetics

The global reaction that are studied are:

$$CH_4 + H_2O \rightleftharpoons 3H_2 + CO \tag{I}$$

$$CO + H_2O \rightleftharpoons H_2 + CO_2 \tag{II}$$

$$CH_4 + 2H_2O \rightleftharpoons 4H_2 + CO_2 \tag{III}$$

The second SMR reaction (III) is often not accounted for assuming it follows directly from combining reactions (I) and (II). As pointed out by Xu and Froment (1989), reaction (III) can, however, proceed via a different reaction mechanism, so that it has to be explicitly accounted for and evaluated [49]. Three possible reaction mechanisms were retained from the literature. Mechanism 1, shown in Fig. 5, is adopted from Xu and Froment [49] and accounts for the second SMR reaction (III) and the presence of adsorbed CH_xO species [66]. Xu and Froment

Table 3
Operating conditions for the steam methane reforming experiments.

Pressure (bar)	1.8–3.6
Temperature (°C)	450–600
H_2O/CH_4 molar	2.9– 5.5
H_2/CH_4 molar	1.25

Table 4
Experimental data.

T (°C)	$W/F^0_{CH_4}$ (g_{cat}.hr/mol)	S/C ratio	x_{CH_4} (%)	x_{CO_2} (%)	Approach to Equilibrium (%)
450	0.803	3.4	0.4	0.4	5.3
450	0.601	3.5	0.3	0.3	5.7
450	1.207	3.5	0.4	0.4	5.9
510	1.166	4.5	4.9	4.4	29.3
510	0.585	3.0	2.0	1.6	15.0
510	1.167	3.0	5.3	4.7	22.9
510	0.585	3.0	1.2	1.0	8.1
550	1.203	3.5	9.5	8.9	28.0
550	0.603	3.5	6.7	6.2	28.3
550	0.804	3.5	8.8	8.2	27.3
570	1.168	2.9	15.0	12.5	34.8
570	1.168	5.5	15.8	13.4	59.9
570	0.585	2.9	8.7	6.6	30.7
600	0.602	3.5	13.4	11.9	44.8
600	0.804	3.5	16.8	15.2	45.7
600	1.207	3.5	20.4	18.2	47.0

[49] showed steps (s7), (s8) and (s9) to be rate determining for respectively reactions (I), (II) and (III), with corresponding rate expressions:

$$r_1 = \frac{\left(k_1/p_{H_2}^{2.5}\right)\left(p_{CH_4}p_{H_2O} - \frac{p_{CO}p_{H_2}^3}{K_I}\right)}{DEN^2} \tag{1}$$

$$r_2 = \frac{\left(k_2/p_{H_2}\right)\left(p_{CO}p_{H_2O} - \frac{p_{H_2}p_{CO_2}}{K_{II}}\right)}{DEN^2} \tag{2}$$

$$r_3 = \frac{\left(k_3/p_{H_2}^{3.5}\right)\left(p_{CH_4}p_{H_2O}^2 - \frac{p_{CO_2}p_{H_2}^4}{K_{III}}\right)}{DEN^2} \tag{3}$$

and with the denominator given by:

$$DEN = 1 + K_{CH_4}p_{CH_4} + K_{CO}p_{CO} + K_{H_2}p_{H_2} + K_{H_2O}\frac{p_{H_2O}}{p_{H_2}} \tag{4}$$

Reduced mechanism 1-red is identical to mechanism 1 but does not account for the second SMR reaction (III), i.e. elementary step (s9). Mechanism 2, shown in Fig. 6, only accounts for the first SMR (I) and water-gas shift reactions (II) and does not consider adsorbed CH_xO species. Adsorbed CO and then CO_2 are assumed to be formed from adsorbed C species. Different rate determining steps can be considered for each of the reaction mechanisms. The corresponding rate equations were then derived following the Langmuir-Hinshelwood-Hougen-Watson approach [51]. Finally, a last kinetic model was adopted from Wei and Iglesia (2004) [67]. From kinetic and isotopic measurements, the rate of the forward steam reforming reaction (I) is assumed proportional to the partial pressure of CH_4 and independent of the partial pressure of the co-reactant. Furthermore, a very low catalyst surface coverage by CO was observed, making competitive adsorption of CO and CH_4 on metal sites unlikely. The co-reactant and the reaction products influence only the extent to which the equilibrium is approached. The net reaction rate can then be written as:

$$r_{nI} = kp_{CH_4}\left(1 - \frac{p_{CO}p_{H_2}^3}{p_{CH_4}p_{H_2O}K_I}\right) \tag{5}$$

Wei and Iglesia (2004) [67] furthermore assumed reaction (III) as a combination of reactions (I) and (II). As written in Eq. (5), the adsorption group, typical for Langmuir-Hinshelwood-Hougen-Watson type rate expressions, is not directly recognized. Eq. (5) can be reformulated as:

$$r_{nI} = \frac{k}{p_{H_2O}}\left(p_{CH_4}p_{H_2O} - \frac{p_{CO}p_{H_2}^3}{K_I}\right) \tag{5bis}$$

Except for the adsorption group, rate Eq. (5 bis) is similar to the rate expression for the first SMR reaction (I) derived by Xu and Froment (1989) [49], Eq. (1), but based on reaction mechanism 1 and rate determining steps (s2) or (s3).

5.2. Methodology

The integral method of kinetic analysis was applied using a non-linear least square analysis based on the minimization of the residual sum of squares of the observed and calculated conversions of methane and carbon dioxide [51,68]. The Athena Visual Studio software was
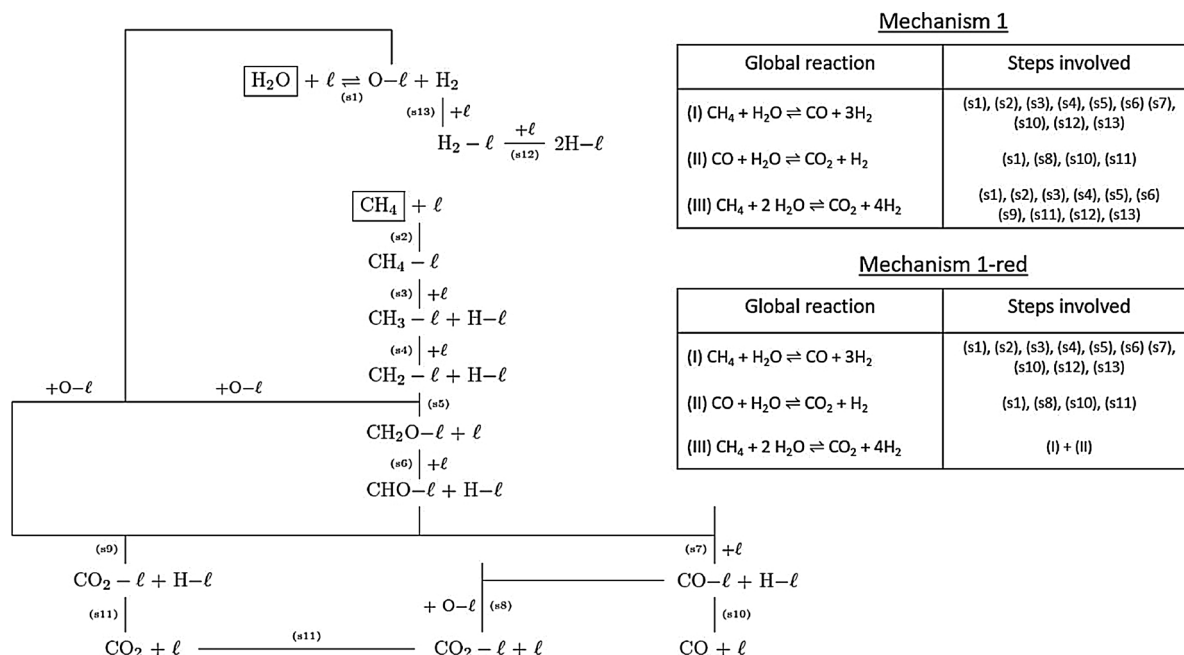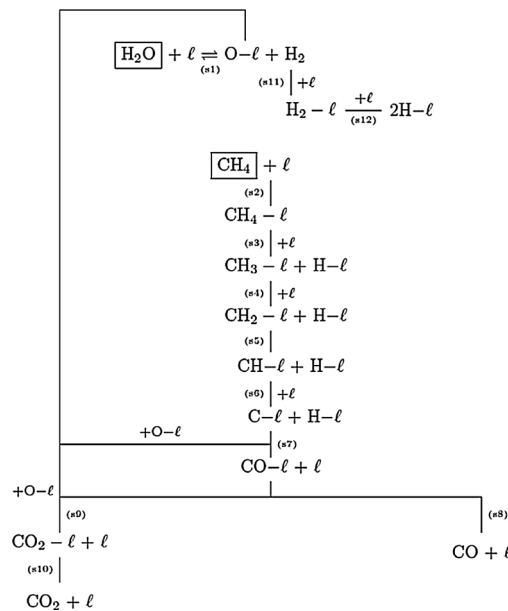

Mechanism 1

Global reaction	Steps involved
(I) $CH_4 + H_2O \rightleftharpoons CO + 3H_2$	(s1), (s2), (s3), (s4), (s5), (s6) (s7), (s10), (s12), (s13)
(II) $CO + H_2O \rightleftharpoons CO_2 + H_2$	(s1), (s8), (s10), (s11)
(III) $CH_4 + 2 H_2O \rightleftharpoons CO_2 + 4H_2$	(s1), (s2), (s3), (s4), (s5), (s6) (s9), (s11), (s12), (s13)

Mechanism 1-red

Global reaction	Steps involved
(I) $CH_4 + H_2O \rightleftharpoons CO + 3H_2$	(s1), (s2), (s3), (s4), (s5), (s6) (s7), (s10), (s12), (s13)
(II) $CO + H_2O \rightleftharpoons CO_2 + H_2$	(s1), (s8), (s10), (s11)
(III) $CH_4 + 2 H_2O \rightleftharpoons CO_2 + 4H_2$	(I) + (II)

Fig. 5. Reaction mechanisms 1 (Xu and Froment, 1989) [49] and 1-red for steam methane reforming.

$$\boxed{H_2O} + \ell \underset{(s1)}{\rightleftharpoons} O-\ell + H_2$$

$$(s11) \Big| +\ell$$

$$H_2 - \ell \xrightarrow[(s12)]{+\ell} 2H-\ell$$

$$\boxed{CH_4} + \ell$$

$$(s2) \Big|$$

$$CH_4 - \ell$$

$$(s3) \Big| +\ell$$

$$CH_3 - \ell + H-\ell$$

$$(s4) \Big| +\ell$$

$$CH_2 - \ell + H-\ell$$

$$(s5) \Big|$$

$$CH-\ell + H-\ell$$

$$(s6) \Big| +\ell$$

$$C-\ell + H-\ell$$

$$+O-\ell \qquad \Big| (s7)$$

$$CO-\ell + \ell$$

$$+O-\ell$$

$$(s9) \qquad\qquad (s8)$$

$$CO_2 - \ell + \ell \qquad\qquad CO + \ell$$

$$(s10) \Big|$$

$$CO_2 + \ell$$

Mechanism 2

Global reaction	Steps involved
(I) $CH_4 + H_2O \rightleftharpoons CO + 3H_2$	(s1), (s2), (s3), (s4), (s5), (s6) (s7), (s8), (s11), (s12)
(II) $CO + H_2O \rightleftharpoons CO_2 + H_2$	(s1), (s8), (s9), (s10)
(III) $CH_4 + 2 H_2O \rightleftharpoons CO_2 + 4H_2$	(I) + (II)

Fig. 6. Reaction mechanism 2 for steam methane reforming. Adapted from Hou and Hughes (2001) [47].

Table 5
Reaction mechanisms and rate determining steps (r.d.s.) tested and model discrimination based on physicochemical and statistical testing.

Mechanism	r.d.s. reaction (I)	r.d.s. reaction (III)	Physicochemical tests	F-value	R^2
1	(s1)	(s1)	Eq. (10) not satisfied	150.7	0.935
1	(s2)	(s1)	Eq. (10) not satisfied	352.7	0.959
1	(s3)	(s1)	Eq. (10) not satisfied	182.7	0.959
1	(s6)	(s1)	Eq. (10) not satisfied	627	0.984
1	(s7)	(s1)	Eqs. (10) and (11) not satisfied	646.4	0.984
1	(s10)	(s1)	Eq. (10) not satisfied	305.9	0.967
1	(s1)	(s2)	Eqs. (10) and (11) not satisfied	292.5	0.949
1	(s2)	(s2)	Eq. (10) not satisfied	268.3	0.962
1	(s3)	(s2)	Eqs. (10) and (11) not satisfied	182.7	0.96
1	(s6)	(s2)	Eqs. (10) and (11) not satisfied	204.7	0.964
1	(s7)	(s2)	Eqs. (10) and (11) not satisfied	203.7	0.964
1	(s10)	(s2)	Eq. (10) not satisfied	306.6	0.975
1	(s1)	(s3)	Eq. (10) not satisfied	228.1	0.956
1	(s2)	(s3)	Eqs. (10) and (11) not satisfied	252.4	0.961
1	(s3)	(s3)	OK	57.6	0.699
1	(s6)	(s3)	Eq. (10) not satisfied	633.1	0.984
1	(s7)	(s3)	Eqs. (10) and (11) not satisfied	646.8	0.984
1	(s10)	(s3)	Eq. (10) not satisfied	399.1	0.974
1	(s1)	(s6)	Eq. (10) not satisfied	633	0.984
1	(s2)	(s6)	Eq. (10) not satisfied	633	0.984
1	(s3)	(s6)	Eq. (10) not satisfied	401.9	0.98
1	(s6)	(s6)	Eq.(10) not satisfied	633.9	0.984
1	(s7)	(s6)	OK	661.4	0.984
1	(s10)	(s6)	Eq. (10) not satisfied	633.1	0.984
1	(s1)	(s9)	Eqs. (10) and (11) not satisfied	365.9	0.972
1	(s2)	(s9)	Eqs. (10) and (11) not satisfied	329.9	0.977
1	(s3)	(s9)	OK	325.5	0.976
1	(s6)	(s9)	Eq. (10) not satisfied	460.5	0.983
1	(s7)	(s9)	OK	447.8	0.977
1	(s10)	(s9)	Eq. (11) not satisfied	295.1	0.974
1-red	(s1)	N.A.	Eq. (10) not satisfied	163.7	0.939
1-red	(s2)	N.A.	Eqs. (10) and (11) not satisfied	283.8	0.965
1-red	(s3)	N.A.	Eqs. (10) and (11) not satisfied	426.5	0.965
1-red	(s6)	N.A.	Eq. (10) not satisfied	561.5	0.981
1-red	(s7)	N.A.	Eq. (11) not satisfied	568.2	0.982
1-red	(10)	N.A.	Eq. (11) not satisfied	199.3	0.944
2	(s2)	N.A.	Eq. (10) not satisfied	106.4	0.731
2	(s3)	N.A.	Eqs. (10) and (11) not satisfied	397.2	0.962
2	(s7)	N.A.	OK	465.5	0.972
2	(s8)	N.A.	OK	343.3	0.947
Wei and Iglesia model (2004) [67]	N.A.	N.A.	Eq. (10) not satisfied	256.6	0.894

used for the parameter estimation and statistical analysis. To calculate these conversions with a specific kinetic model, the set of species continuity equations for CH_4 and CO_2 were integrated using a fourth-order Runge-Kutta routine. Let x_{CH_4} and x_{CO_2} be the conversion of methane and carbon dioxide respectively:

$$x_{CH_4} = \frac{F^0_{CH_4} - F_{CH_4}}{F^0_{CH_4}} \quad x_{CO_2} = \frac{F_{CO_2}}{F^0_{CH_4}}$$

The species continuity equations are ordinary differential equations that can be written:

$$\frac{dx_{CH_4}}{d\left(\frac{W}{F^0_{CH_4}}\right)} = r_{CH_4} \tag{6}$$

$$\frac{dx_{CO_2}}{d\left(\frac{W}{F^0_{CH_4}}\right)} = r_{CO_2} \tag{7}$$

The parameter estimation was based on data at different temperatures using non-linear least squares regression. To reduce the effect of a high correlation between pre-exponential factors and activation energies or adsorption enthalpies on the regression, the rate and adsorption constants were reparametrized:

$$k_i = A(k_i)\exp\left(-\frac{E_{ai}}{RT}\right) = k_{i,T_m}\exp\left\{-\frac{E_{ai}}{R}\left(\frac{1}{T} - \frac{1}{T_m}\right)\right\} \tag{8}$$

$$K_A = A(K_A)\exp\left(-\frac{\Delta H_A}{RT}\right) = K_{A,T_m}\exp\left\{-\frac{\Delta H_A}{R}\left(\frac{1}{T} - \frac{1}{T_m}\right)\right\} \tag{9}$$

Model discrimination was based on physicochemical and statistical testing. For the physicochemical testing, thermodynamics imposes that $\Delta H = \overrightarrow{E_a} - \overleftarrow{E_a}$. For endothermic reactions, this leads to:

$$E_a > |\Delta H| \tag{10}$$

Note that with few exceptions [49,69–72], values for the activation energies not respecting criterion (10) are reported in the literature. Since adsorption reduces the entropy of the system, a thermodynamic criterion for the adsorption constants is:

$$\Delta S^0_j < 0 \leftrightarrow A(S_j) = \exp[\Delta S^0_j/R] < 1 \tag{11}$$

Furthermore, for non-dissociative adsorption [73]:

$$-\Delta S^0_{j,a} < S^0_{j,g} \tag{12}$$

The sets of rate equations with parameters satisfying criteria (10) to (12) were retained and the others eliminated. Statistical tests were applied for further model discrimination [51,68]. The F-test was used to compare the model adequacy. The significance of the estimated parameters was tested and the 95% confidence intervals calculated by means of the t-test.

During the steam reforming experiments, the water-gas shift (WGS) reaction approaches equilibrium, so that a statistically significant value for k_2 cannot be estimated. Therefore, the rate expression and constant of Xu and Froment (1989) were adopted for the WGS reaction. In a commercial steam reformer, the WGS reaction will typically also

Table 6
Parameter estimates for the retained kinetic model for use with partial pressures in bar and reaction rates in mol/kg_{cat}.s.

(a)-Model A

Parameter	Value	Unit	t-value	95% Confidence intervals
$A(k_1)$	5.23×10^{23}	mol. $bar^{1/2}/(kg_{cat}. s)$	17.4	$5.23 \pm 0.62\,(\times 10^{23})$
$A(k_2)$	5.43×10^5	mol/(kg_{cat}. s. bar)		Xu and Froment [49]
$A(k_3)$	1.66×10^{24}	mol. $bar^{1/2}/(kg_{cat}. s)$	29.89	$1.66 \pm 0.12\,(\times 10^{24})$
E_{a1}	291.4	kJ/mol	49.99	291.4 ± 11.9
E_{a2}	67.13	kJ/mol		Xu and Froment [49]
E_{a3}	301.1	kJ/mol	87.39	301.1 ± 7.1
$A(K_{H_2O})$	5.8×10^8		93.62	$5.8 \pm 0.059\,(\times 10^8)$
ΔH_{H_2O}	88.68	kJ/mol		Xu and Froment [49]
$A(K_{CH_4})$	4.71×10^{-3}	bar^{-1}	0.43	$4.71 \pm 3.68\,(\times 10^{-3})$
ΔH_{CH_4}	-38.28	kJ/mol		Xu and Froment [49]
$A(K_{CO})$	8.23×10^{-5}	bar^{-1}		"
ΔH_{CO}	-70.65	kJ/mol		"
$A(K_{H_2})$	6.12×10^{-9}	bar^{-1}		"
ΔH_{H_2}	-82.90	kJ/mol		"

(b)-Model B

Parameter	Value	Unit	t-value	95% Confidence intervals
$A(k_1)$	7.48×10^{12}	mol. $bar^{1/2}/(kg_{cat}. s)$	27.98	$7.48 \pm 0.54\,(\times 10^{12})$
$A(k_2)$	5.43×10^5	mol/(kg_{cat}. s. bar)		Xu and Froment [49]
$A(k_3)$	9.56×10^{11}	mol/(kg_{cat}. s)	28.43	$9.56 \pm 0.68\,(\times 10^{11})$
E_{a1}	226.4	kJ/mol	60.16	226.4 ± 7.5
E_{a2}	67.13	kJ/mol		Xu and Froment [49]
E_{a3}	210.4	kJ/mol	59.03	210.4 ± 7.2
$A(K_{H_2O})$	2.09×10^5		71.29	$2.09 \pm 0.06\,(\times 10^5)$
ΔH_{H_2O}	88.68	kJ/mol		Xu and Froment [49]
$A(K_{CH_4})$	2.68×10^{-4}	bar^{-1}	1.2	$2.68 \pm 2.03\,(\times 10^{-4})$
ΔH_{CH_4}	-38.28	kJ/mol		Xu and Froment [49]
$A(K_{CO})$	8.23×10^{-5}	bar^{-1}		"
ΔH_{CO}	-70.65	kJ/mol		"
$A(K_{H_2})$	6.12×10^{-9}	bar^{-1}		"
ΔH_{H_2}	-82.90	kJ/mol		"

rapidly approach equilibrium [25]. An accurate description of the WGS reaction kinetics is then not essential for reactor simulation. Because of the very low partial pressure of CO and very low value of K_{H_2} at the experimentally tested temperatures, K_{H_2} and K_{CO} were also not re-estimated. Finally, the assumption was made that the adsorption enthalpies are equal to those with the conventional SMR catalyst so that only the pre-exponential entropic terms for K_{CH_4} and K_{H_2O} were re-estimated. The total number of parameters to be estimated was as such limited to 6 for the reaction mechanism 1 (Fig. 5), to 4 for the reaction mechanism 2 (Fig. 6) and to 2 for the Wei and Iglesia (2004) model.

6. Parameter estimation and model discrimination

The experimental data used for the parameter estimation and statistical testing are shown in Table 4. A total of 41 sets of rate equations, derived assuming a certain reaction mechanism with given rate determining steps, were tested as shown in Table 5. For only six sets of rate equations, the estimated rate parameters respected criteria (10) to (12). Based on the F-test and the R^2 value, two competitive models were retained. The first model (model A) is identical to the one proposed by Xu and Froment (1989) for the conventional SMR catalyst [49], i.e. mechanism 1 with rate determining steps (s7) and (s9) for reactions (I) and (III) respectively - viz Eqs. (1)–(4). The F-value obtained with model A is 447.8, the R^2-value is 0.977. The rate parameters and their corresponding 95% confidence intervals are given in Table 6-a, for use of the rate expressions (1), (2) and (3) with partial pressures in bar and reaction rates in mol/(kg$_{cat}$.s). Note that kg$_{cat}$ refers to the catalytically active intermediate and external layers. The variance-covariance matrix of the parameters showed that the correlations between the different model parameters were all significantly below 0.95, except for $A(k_3)$ and (K_{H_2O}) with a correlation of 0.996.

The second model (model B), with the highest F and R^2 values of

respectively 661.4 and 0.984, is also based on reaction mechanism 1 (Fig. 5) but with rate determining steps (s7) and (s6) for reactions (I) and (III) respectively. The rate equation of reaction (III) then becomes:

$$r_3 = \frac{\left(k_3 \big/ p_{H_2O} p_{H_2}^2 \right)\left(p_{CH_4} p_{H_2O}^2 - \frac{p_{CO_2} p_{H_2}^4}{K_{III}} \right)}{DEN^2}$$ (3-bis)

The rate parameters and 95% confidence intervals are given in Table 6-b, for use of the rate expressions (1), (2) and (3-bis). The denominator is identical and given by Eq. (4). The correlations between the different model parameters were all significantly below 0.95 and in general less than with model A. Only for the correlation between E_{a1} and E_{a3} a value of 0.971 was found. Although the rate determining step for reaction (III) is (s6), which is also an elementary step in the mechanism of reaction (I), it was found necessary to account for CO_2 and H_2 formation through reaction (III). None of the tested models based on reaction mechanism 1-red was found to respect criteria (10) to (12).

The observed and predicted conversions of methane and carbon dioxide are compared in Fig. 7 for the two retained models. The reaction enthalpies of the steam reforming reactions do not exceed 225 kJ/mol for reaction (I) and 196 kJ/mol for reaction (III) over the whole temperature range (experimentally tested and industrially practiced), so that the values for activation energies given in Table 6-a and 6-b satisfy criterion (10). For the adsorption constant of methane, the standard entropy of methane at 25 °C is 186.1 J/(mol.K), so that criterion (12)

$$A(K_{CH_4}) = \exp\left(\frac{\Delta S^0_{CH_4,a}}{R} \right) > \exp\left(\frac{-S^0_{CH_4,g}}{R} \right) = 1.9027 \times 10^{-10}$$ (13)

is also satisfied over the whole temperature range for the two models. Regarding the adsorption constant of steam, the value of $A(K_{H_2O})$ does
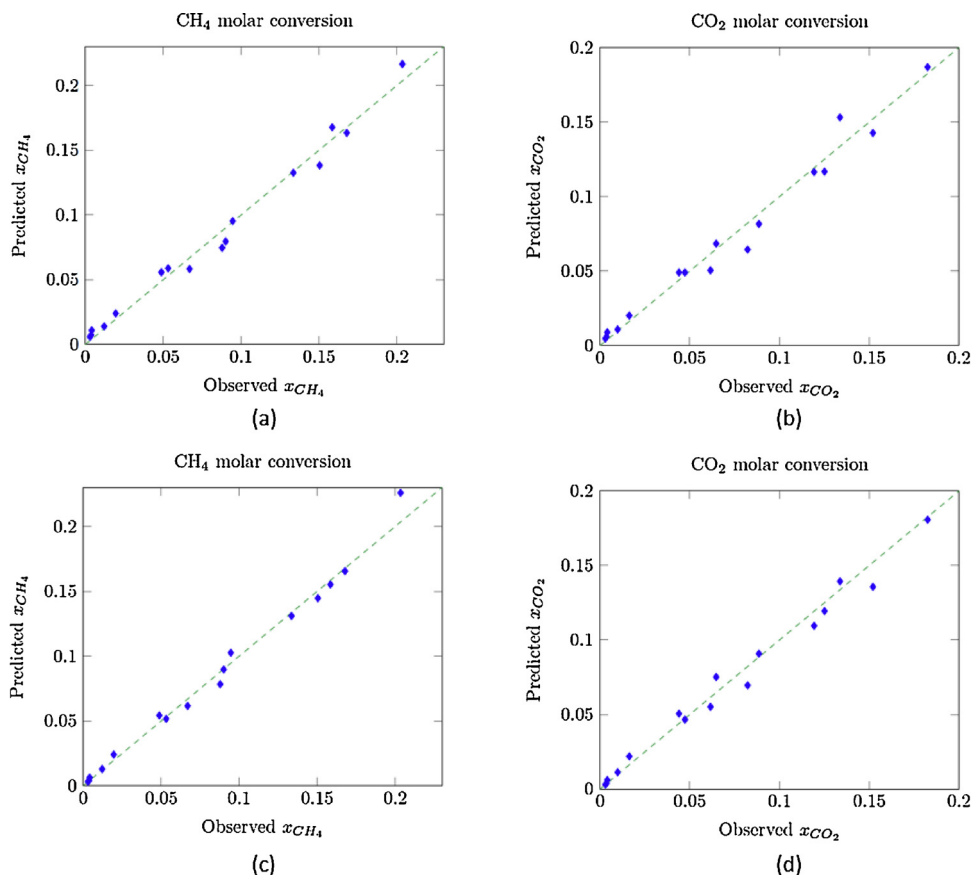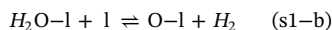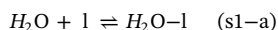

Fig. 7. Parity plots for the molar conversion of CH$_4$ and CO$_2$ with (a)-(b) model A and (c)-(d) model B.

not satisfy equation (11). Because step (s1) in the reaction mechanism 1 in Fig. 5 combines two elementary steps:

$$H_2O + l \rightleftharpoons H_2O-l \quad (s1-a)$$

$$H_2O-l + l \rightleftharpoons O-l + H_2 \quad (s1-b)$$

and K_{H_2O} is defined by:

$$K_{H_2O} = \frac{p_{H_2} \cdot C_{O-\ell}}{p_{H_2O} \cdot C_\ell} \quad (14)$$

this term is, however, not the true adsorption constant of steam and is not necessarily subject to the van't Hoff equation and thermodynamic constraints (11) and (12).

A comparison between the rate parameters of a conventional SMR catalyst (Xu and Froment 1989) and the ASC catalyst coating is presented in the form of a Van't Hoff / Arrhenius diagram, in Fig. 8-a for the model A and in Fig. 8-b for the model B [49]. The temperature range covers the temperatures experimentally tested ($1.15 < 1000/T < 1.3$) and commercially applied. Note that a steam reformer operates typically between 500 and 800 °C while a dry-reformer operates at higher temperatures, between 600 and 1000 °C.

Fig. 8-a shows that the differences in the values of the rate parameters for model A mainly come from the pre-exponential factors of the rate constants that are related to the total concentration of active sites. In the entire temperature range, significantly higher values for k_1 and even more for k_3 are obtained for the ASC catalyst than for the conventional catalyst (Xu and Froment, 1989). For example, the value of k_3 for the ASC catalyst is around 7 orders of magnitude higher than k_3 for the conventional catalyst. The k_1 factors are closer, with ASC k_1 being 6 orders of magnitude higher than for the conventional catalyst. In practice, this potentially higher selectivity towards the formation of CO_2 and H_2 is of course affected by the WGS reaction that typically approaches equilibrium in a commercial reformer. Per kilogram of catalyst, the ASC catalyst contains, however, around 75 wt.% nickel, whereas the conventional magnesium spinel-supported catalyst only 15 wt.% (Xu and Froment, 1989). The net reaction rates are not only determined by the rate constants k_1 and k_3, but also by the values of the adsorption constants – see Eqs. (1)–(4). Fig. 8 shows values for K_{CH4} and K_{H2O} that are significantly higher, i.e. 7.1 and 3277 times higher respectively, for the ASC than for the conventional catalyst over the entire considered temperature range. As a result, with model A, the ASC catalyst is intrinsically much more active than the conventional catalyst, but the reactions are strongly inhibited by steam, due to a large coverage of the catalyst surface by adsorbed oxygen atoms.

Fig. 8-b shows that for model B, the value of k_1 is around 30 times lower for the ASC catalyst than for the conventional catalyst over the

whole temperature range. For k_3, similar values are found over the experimentally tested temperature range and values less than 10 times lower than for the conventional catalyst are predicted at typical industrially practiced temperatures. This again leads to a potentially higher selectivity for CO_2 and H_2. The ASC catalyst is as such intrinsically slightly less active than the conventional catalyst. With model B, the adsorption constants K_{CH4} and K_{H2O} have values very close to the ones estimated by Xu and Froment (1989), however. The reactions are, hence, much less inhibited by steam than in model A. The higher F and R^2-vaules are in favour of model B.

7. Optimal coating thickness

The catalyst effectiveness was evaluated by calculating species concentration profiles inside the catalyst layer under typical operating conditions. The species continuity equations in the catalyst are written [51] :

$$\frac{d}{d\xi}\left(D_{e,CH_4} \frac{dp_{s,CH_4}}{d\xi}\right) = 10^{-5}RT. h^2. r_{CH_4}(p_{s,j}). \rho_s \quad (15a)$$

$$\frac{d}{d\xi}\left(D_{e,CO_2} \frac{dp_{s,CO_2}}{d\xi}\right) = 10^{-5}RT. h^2. r_{CO_2}(p_{s,j}). \rho_s \quad (15b)$$

with the corresponding boundary conditions:

$$\frac{dp_{s,CH_4}}{d\xi} = \frac{dp_{s,CO_2}}{d\xi} = 0 \ at \ \xi = 0$$

$$p_{s,CH_4} = p_{CH_4} \ ; \ p_{s,CO_2} = p_{CO_2} \ at \ \xi = 1$$

and ξ the dimensionless intra-catalyst coordinate and partial pressures in bar.

The reaction rates are given by Eqs. (1)–(3) for model A and Eqs. (1), (2) and (3-bis) for model B. The effectiveness factor for a given global reaction can be calculated from:

$$\eta_i = \frac{\int_0^1 r_i(p_{s,j}) \, d\xi}{r_i(p_j)} \quad (16)$$

The species effective diffusivity is calculated from:

$$D_{e,A} = \frac{\varepsilon_s}{\tau}\overline{D_A} \quad (17)$$

The tortuosity factor τ accounts for the tortuous nature of the pores and eventual pore constrictions [51]. Values ranging from 2 to 5 were reported in the literature [70,74–77]. Kolitcheff et al. [78] reported different correlations to calculate the tortuosity from the catalyst
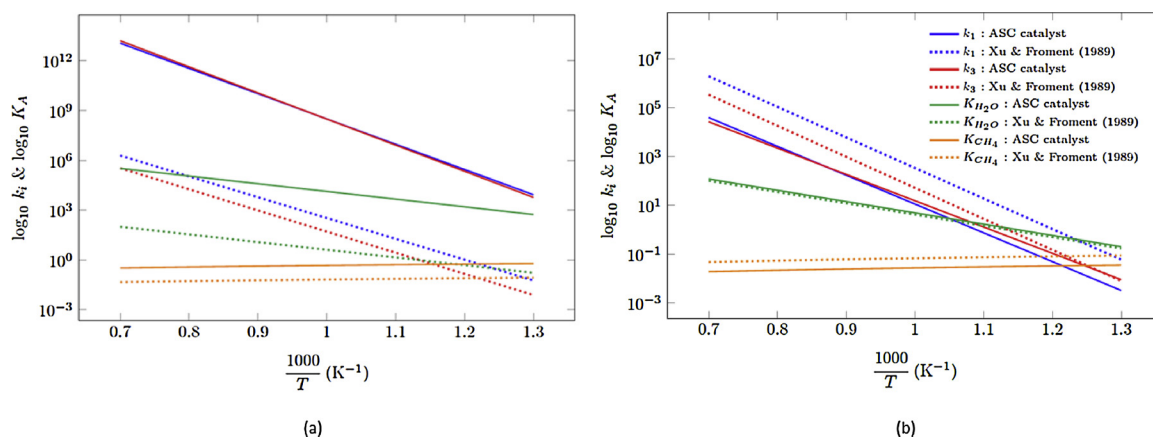

Fig. 8. Arrhenius / Van't Hoff diagrams: comparison of the rate parameters with a conventional catalyst and with the ASC catalyst coating for (a) model A and (b) model B respectively. Rate constants k_i in mol. bar$^{1/2}$/(kg$_{cat}$.s) or mol/(kg$_{cat}$.s) and adsorption constants K_A in bar^{-1} (For interpretation of the references to colour in this figure legend, the reader is referred to the web version of this article.).
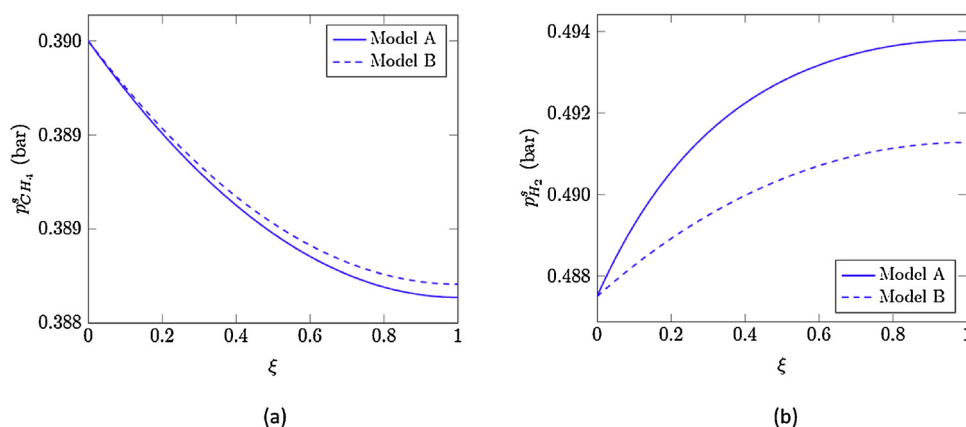
Fig. 9. Partial pressure profiles of (a) CH_4 and (b) H_2 inside a 10 μm catalyst coating under typical experimental reaction conditions (T = 550 °C, P = 3 bar, y_{CH4} = 0.13, y_{CO} = 0.01, y_{CO2} = 0.04, S/C = 4.4, H_2/C = 1.25).
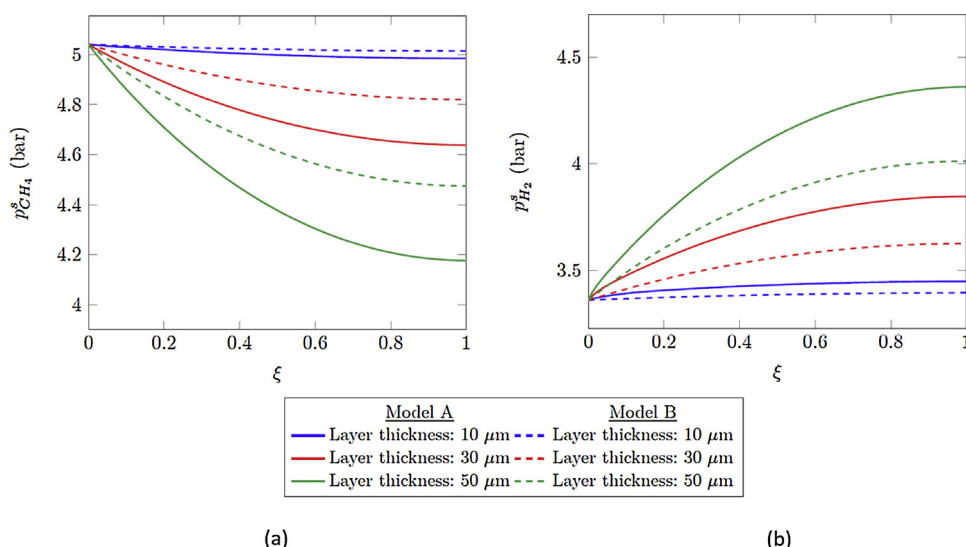

Fig. 10. Partial pressure profiles of (a) CH_4 and (b) H_2 inside catalyst coatings of different thickness under typical commercial SMR operating conditions (T = 700 °C, P = 28 bar, y_{CH4} = 0.18, y_{H20} = 0.6, y_{H2} = 0.12, y_{CO} = 0.01, y_{CO2} = 0.05) with models A (solid lines) and B (dashed lines) and (c) related catalyst effectiveness factors for the two global SMR reactions.

Layer thickness	Model A		Model B	
	η_I	η_{III}	η_I	η_{III}
10 μm	0.959	0.909	0.995	0.998
30 μm	0.784	0.620	0.954	0.978
50 μm	0.606	0.454	0.884	0.937

(c)

porosity. For the measured ASC catalyst coating porosity of 0.084, these correlations [79–82] give values of τ between 1.4 and 3.6. For a conventional Ni/MgAl$_2$O$_4$ catalyst with a porosity of 0.52, Xu and Froment (1989) found, however, a value of 3.54 [25]. Therefore, a value of τ = 4 was considered for the ASC catalyst coating. The diffusivity of the reacting species A are calculated from the molecular and Knudsen diffusivities:

$$D_A(r_p) = \left(\frac{1}{D_{mA}} + \frac{1}{D_{kA}(r_p)} \right)^{-1}$$
(18)

From the pore size distribution given in Fig. 3, the average diffusivity of species A is given by:

$$\overline{D_A} = \sum_i D_A(r_{p,i}) . S(r_{p,i})$$
(19)

where $S(r_{p,i})$ is the void volume fraction taken by the pores with radii ranging from $r_{p,i}$ to $r_{p,i+1}$.

The profiles of the species partial pressures inside the catalyst coating and corresponding effectiveness factors for a 7 μm coating under typical experimentally tested operating conditions are shown in Fig. 9. With kinetic model A, the effectiveness factors, calculated by Eq. (16), are η_I = 1.028 for the first SMR reaction (I) and η_{III} = 0.98 for the second SMR reaction (III). With model B, η_I = 1.013 for reaction (I) and η_{III} = 1.003 for reaction III. This confirms that experiments were carried out under conditions of negligible intra-catalyst diffusion limitations.

The influence of the catalyst coating thickness was studied under typical commercial steam methane reforming operating conditions. Fig. 10 shows the calculated species partial pressure profiles in catalyst coatings of 10, 30 and 50 μm respectively, calculated with the two retained kinetic models. Under the given conditions, significant intra-catalyst diffusion limitations are observed with model A in the 30 μm
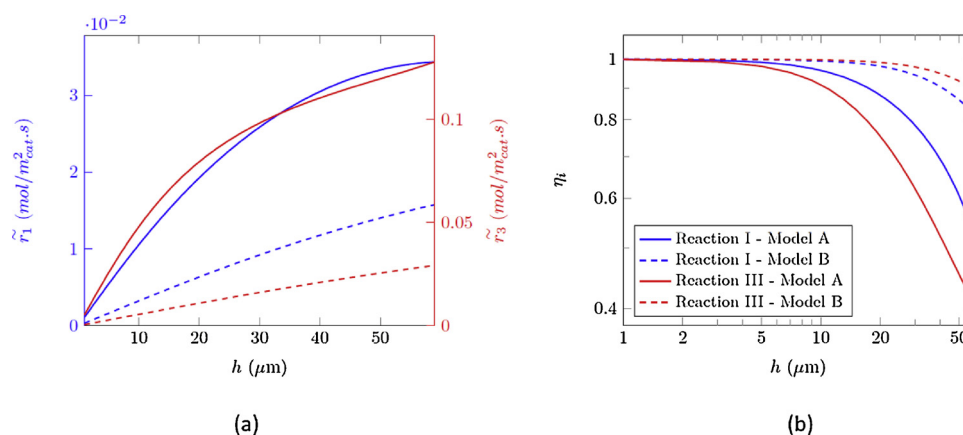
Fig. 11. (a) Observed reaction rates and (b) effectiveness factors for the two global SMR reactions (log-log), as a function of the catalyst coating thickness. Typical commercial SMR operating conditions as in Fig. 10.

and 50 μm catalyst coatings. Diffusion limitations are also observed with model B, but to less extent. Fig. 11 shows (a) the observed (or average) reaction rates in $mol/m_{cat}^2.s$:

$$\widetilde{r}_i = \eta_i h \rho_s . r_{i,s}^s \qquad (20)$$

and (b) the catalyst effectiveness factors as a function of the catalyst coating thickness with the two kinetic models. Under the given conditions and for model A, η becomes proportional to $1/h$ for both SMR reactions when the catalyst coating thickness exceeds 40 μm, so that increasing the catalyst coating thickness has a negligible effect on the observed conversion. The behavior is different for model B for which increasing the coating thickness beyond 40 μm is still favorable on the observed conversions, the effectiveness factor being close to 1 for a coating thickness up to 50 μm.

8. Conclusions

An experimental study of the intrinsic kinetics of steam methane reforming (SMR) on an adherent nickel-based coating on a metal substrate from Alloy Surfaces, Co. Inc. (ASC) was carried out. SEM and N_2 adsorption/desorption characterizations revealed inner and outer coatings measuring an average of 7 and 40 μm respectively with a BET average area of 7.4 m^2/g, porosity of 0.084 and Ni content of 75–85 wt %. EDX, XRD and TPR analysis indicated formation of a very thin NiO passivation layer upon contact with air. An experimental fixed bed reactor was designed and operating conditions selected to guarantee measurements of the intrinsic reaction kinetics. Discrimination between different kinetic models and the corresponding sets of rate equations followed from physicochemical and statistical testing. Two possible models were retained, both based on the reaction mechanism of Xu and Froment (1989) [49] with a second SMR reaction forming CO_2 and H_2 and CO and CO_2 formation through CH_xO surface species. The first model confirms the rate determining steps proposed by Xu and Froment (1989) [49]. The estimated rate parameters for the ASC catalyst coating show that it is intrinsically more active than the conventional SMR catalyst, but the reactions are inhibited by strong adsorption of steam. The second model indicates a different rate determining step for the second SMR reaction. The estimated parameters show the ASC catalyst coating to be intrinsically somewhat less active than the conventional SMR catalyst. Adsorption constants are, however, more in line with those determined by Xu and Froment (1989) and the reactions are much less inhibited by adsorption of steam. Therefore, and based on the statistical testing, the second model is finally favored. Simulations of the intra-catalyst diffusion-reaction under typical commercial SMR conditions show that for the two SMR reactions, catalyst effectiveness factors close to 1 are possible with a catalyst coating thickness of up to 50 μm. Finally, both under the experimental conditions studied and

under typical commercial SMR conditions and in contrast to what was observed with a conventional SMR catalyst, the ASC catalyst is nearly equally or more active for the second SMR reaction, producing CO_2 and H_2, than for the first SMR reaction, producing CO and H_2.

References

[1] F. Barbir, Transition to renewable energy systems with hydrogen as an energy carrier, Energy 34 (2009) 308–312.
[2] B. Zhou, M. Schulz, H.Y. Lin, S.I. Shah, J. Qu, C.P. Huang, Photoelectrochemical generation of hydrogen over carbon-doped TiO_2 photoanode, Appl. Catal. B 92 (2009) 41–49.
[3] Q. De Radiguès, R. Santoro, J. Proost, Kinetic transitions during Ag and Cu electrorecovery on reticulated vitreous carbon electrodes in flow-by mode, Chem. Eng. J. 162 (2010) 273–277.
[4] M. Altomare, M. Pozzi, M. Allieta, L.G. Bettini, E. Selli, H_2 and O_2 photocatalytic production on TiO_2 nanotube arrays: effect of the anodization time on structural features and photactivity, Appl. Catal. B 136-137 (2013) 81–88.
[5] P. Lianos, Review of recent trends in photoelectrocatalytic conversion of solar energy to electricity and hydrogen, Appl. Catal. B 210 (2017) 235–254.
[6] X.Q. Peng, D. Xue, S.Z. Zhan, C.L. Ni, Visible-light-driven photocatalytic system based on a nickel complex over CdS materials for hydrogen production from water, Appl. Catal. B 219 (2017) 353–361.
[7] J.F. Guayaquil-Sosa, B. Serrano-Rosales, P.J. Valadés-Pelayo, H. de Lasa, Photocatalytic hydrogen production using mesoporous TiO_2 doped with Pt, Appl. Catal. B 211 (2017) 337–348.
[8] M. Wen, K. Mori, Y. Kuwahara, T. An, H. Yamashita, Design and architecture of metal organic frameworks for visible light enhanced hydrogen production, Appl. Catal. B 218 (2017) 555–569.
[9] E.S. Lox, G.F. Froment, Kinetics of the Fischer-Tropsch reaction on a precipitated promoted iron catalyst. 1. Experimental procedure and results, Ind. Eng. Chem. Res. 32 (1993) 61–70.
[10] E.S. Lox, G.F. Froment, Kinetics of the Fischer-Tropsch reaction on a precipitated promoted iron catalyst. 2. Kinetic modeling, Ind. Eng. Chem. Res. 32 (1993) 71–82.
[11] M. Saeys, K.F. Tan, J. Chang, A. Brogna, Improving the stability of cobalt Fischer-Tropsch catalysts by boron promotion, Ind. Eng. Chem. Res. 49 (2010) 11098–11100.
[12] K.F. Tan, J. Xu, J. Chang, A. Borna, M. Saeys, Carbon deposition on Co catalysts during Fischer-Tropsch synthesis: a computational and experimental study, J. Catal. 274 (2010) 121–129.
[13] S.-H. Kang, J.W. Bae, J.-Y. Cheon, Y.-J. Lee, K.-S. Ha, K.-W. Jun, D.-H. Lee, B.-W. Kim, Catalytic performance on iron-based Fischer-Tropsch catalyst in fixed-bed and bubbling fluidized-bed reactor, Appl. Catal. B 103 (2011) 169–180.

[14] M. Gharibi, F.T. Zangeneh, F. Yaripour, S. Sahbdelfar, Nanocatalysts for conversion of natural gas to liquid fuels and petrochemical feedstocks, Appl. Catal. A 443-444 (2012) 8–26.

[15] V.R. Choudhary, K.C. Mondal, CO_2 reforming of methane combined with steam reforming or partial oxidation of methane to syngas over $NdCoO_3$ perovskite-type mixed metal-oxide catalyst, Appl. Energy 83 (2006) 1024–1032.

[16] S. Damyanova, B. Pawelec, K. Arishtirova, M.V.M. Huerta, J.L.G. Fierro, The effect of CeO_2 on the surface and catalytic properties of Pt/CeO_2-ZrO_2 catalysts for methane dry reforming, Appl. Catal. B 89 (2009) 149–159.

[17] A.L.M. Da Silva, L.B. Mattos, J.P. Den Breejen, J.H. Bitter, K.P. De Jong, F.B. Noronha, Oxidative steam reforming of ethanol over carbon nanofiber supported Co catalysts, Catal. Today 164 (2011) 262–267.

[18] N.H. Elsayed, N.R.M. Roberts, B. Joseph, J.N. Kuhn, Low temperature dry reforming of methane over Pt-Ni-Mg/ceria zirconia catalysts, Appl. Catal. B 179 (2015) 213–219.

[19] W. Taifan, J. Baltrusaitis, CH_4 conversion to value added products: potential, limitations and extensions of a single step heterogeneous catalysis, Appl. Catal. B 198 (2016) 525–547.

[20] T. Stroud, T.J. Smith, E. Le Saché, J.L. Santos, M.A. Centeno, H. Arellano-Garcia, J.A. Ordriozola, T.R. Reina, Chemical CO_2 recyling via dry and bi reforming of methane using Ni-Sn/Al_2O_3 and Ni-Sn/CeO_2-Al_2O_3 catalysts, Appl. Catal., B 224 (2018) 125–135.

[21] E. McFarland, Unconventional chemistry for unconventional natural gas, Science 338 (2012) 341–342.

[22] W. Liss, Demand outlook: a golden age of natural gas, Chem. Eng. Prog. 108 (2012) 35–40.

[23] W.E. Liss, Impacts of shale gas advancements on natural gas utilization in the United States, Energy Technol. 2 (2014) 953–967.

[24] H. Hu, R. Green, Making markets for hydrogen vehicles: lessons from LPG, Int. J. Hydrogen Energy 36 (2011) 6399–6406.

[25] J. Xu, G.F. Froment, Methane steam reforming: II. Diffusional limitations and reactor simulation, AIChE J. 35 (1989) 97–103.

[26] S. Ratan, M.P. Ralston, J. De Wilde, Novel approach to ammonia plant revamps with ZoneFlow™ reactor technology, nitrogen + syngas 2018, Conference Proceedings, Gothenburg, Sweden, 2018.

[27] J. De Wilde, G.F. Froment, Computational fluid dynamics in chemical reactor analysis and design: application to the ZoneFlow™ reactor for methane steam reforming, Fuel 100 (2012) 48–56.

[28] J. De Wilde, G.F. Froment, Modeling of dual-zone structured reactors for natural gas steam reforming, Ind. Eng. Chem. Res. 52 (2013) 14055–14065.

[29] P. Avila, M. Montes, E.E. Miro, Monolithic reactors for environmental applications: a review on preparation technologies, Chem. Eng. Sci. 109 (2005) 11–36.

[30] E.D. Banus, V.G. Milt, E.E. Miro, M.A. Ulla, Structured catalyst for the catalytic combustion of soot: $Co,Ba,K/ZrO_2$ supported on Al_2O_3 foam, Appl. Catal. A 362 (2009) 129–138.

[31] L.C. Almeida, F.J. Echave, O. Sanz, M.A. Centeno, J.A. Odriozola, M. Montes, Washcoating of metallic monoliths and microchannel reactors, Stud. Surf. Sci. Catal. 175 (2010) 25–33.

[32] H. Pennemann, M. Dobra, M. Wichert, G. Kolb, Optimizaton of wash-coating slurries as catalyst carrier for screen printing into microstructured reactors, Chem. Eng. Technol. 36 (2013) 1033–1041.

[33] S. Danaci, L. Protasova, J. Lefevere, L. Bedel, R. Guilet, P. Marty, Efficient CO_2 methanation of Ni/Al_2O_3 coated structured catalysts, Catal. Today 273 (2016) 234–243.

[34] V. Meille, Review on methods to deposit catalysts on structured surfaces, Appl. Catal. A 315 (2006) 1–17.

[35] X. Zhai, S. Ding, Z. Liu, Y. Jin, Y. Cheng, Catalytic performance of Ni catalysts for steam reforming of methane at high space velocity, Int. J. Hydrogen Energy 36 (2011) 482–489.

[36] Z. Liu, B. Chu, X. Zhai, Y. Jin, Y. Cheng, Total methanation of syngas to synthetic natural gas over Ni catalyst in a micro-channel reactor, Fuel 95 (2012) 599–605.

[37] C. Rallan, A. Garforth, Growth of hierarchically structured high-surface area alumina on FeCralloy® rods, Chin. J. Chem. Eng. 22 (2014) 861–868.

[38] A. Vita, G. Cristiano, C. Italiano, L. Pino, S. Specchia, Syngas production by methane oxy-steam reforming on $Me/CeO2$ (Me = Rh, Pt, Ni) catalyst lined on cordierite monoliths, Appl. Catal. B 162 (2015) 551–563.

[39] A. Obradovic, B. Likozar, J. Levec, Catalytic surface development of novel nickel plate catalyst with combined thermally annealed platinum and alumina coatings for steam methane reforming, Int. J. Hydrogen Energy 38 (2013) 1419–1429.

[40] W.E. Windes, J. Zimmerman, I.E. Reimanis, Electrophoretic deposition applied to thick metal-ceramic coatings, Surf. Coat. Technol. 157 (2002) 267–273.

[41] Y.-H. Chin, J. Hu, C. Cao, Y. Gao, Y. Wang, Preparation of a novel structured catalyst based on aligned carbon nanotube arrays for a microchannel Fischer-Tropsch synthesis reactor, Catal. Today 110 (2005) 47–52.

[42] V.A. Durante, R. Gill, A. Davis, E.C. Soltani, Metal-Supported Catalyst Structures and Processes for Manufacturing the Same, U.S. Patent 9, US 2016/0354767 A1 (2016).

[43] J. Zielinski, Morphology of nickel/alumina catalysts, J. Catal. 76 (1982) 157–163.

[44] C. Li, Y.W. Chen, Temperature-programmed-reduction studies of nickel oxide/alumina catalysts: effects of the preparation method, Thermochim. Acta 256 (1995) 457–465.

[45] J.R.H. Ross, M.C.F. Steel, Mechanism of the steam reforming of methane over a coprecipitated nickel-alumina catalyst, J. Chem. Soc., Faraday Trans. 1. 69 (1973) 10–21.

[46] S. Sepehri, M. Rezaei, G. Garbarino, G. Busca, Facile synthesis of a mesoporous alumina and its application as a support of Ni-based autothermal reforming catalysts, Int. J. Hydrogen Energy 41 (2016) 3456–3464.

[47] K. Hou, R. Hughes, The kinetics of methane steam reforming over a Ni/α-Al_2O catalyst, Chem. Eng. J. 82 (2001) 311–328.

[48] X. Yang, An experimental investigation on the deactivation and regeneration of a steam reforming catalyst, Renew. Energy 112 (2017) 17–24.

[49] J. Xu, G.F. Froment, Methane steam reforming, methanation and water-gas shift: I. Intrinsic kinetics, AIChE J. 35 (1989) 88–96.

[50] M.A. Lugo-Pimentel, A New Thin Layered Structural Coating on a Metal Substrate for Enhanced Hydrogen Production from Steam Methane Reforming (MSc Thesis), CUNY City College, New York, 2017 https://academicworks.cuny.edu/cc_etds_theses/672/.

[51] G.F. Froment, K.B. Bischoff, J. De Wilde, Chemical Reactor Analysis and Design, third ed., John Wiley & Sons, Inc, Hoboken, 2010.

[52] J.J. Carberry, Chemical and Catalytic Reaction Engineering, McGraw-Hill, New York, 1976.

[53] J.J. Carberry, M. Wendel, A computer model of the fixed bed catalytic reactor: the adiabatic and quasi-adiabatic cases, AIChE J. 9 (1963) 129–133.

[54] L.C. Young, B.A. Finlayson, Axial dispersion in nonisothermal packed bed chemical reactors, Ind. Eng. Chem. Fundam. 12 (1973) 412–422.

[55] C.F. Chu, K.M. Ng, Flow in packed tubes with a small tube to particle diameter ratio, AIChE J. 35 (1989) 148–158.

[56] D.E. Mears, Diagnostic criteria for heat transport limitations in fixed bed reactors, J. Catal. 20 (1971) 127–131.

[57] D.E. Mears, Tests for transport limitations in experimental catalytic reactors, Ind. Eng. Chem. Proc. Des. Dev. 10 (1971) 541–547.

[58] A.P. de Wasch, G.F. Froment, Heat transfer in packed beds, Chem. Eng. Sci. 27 (1972) 567–576.

[59] R.J. Berger, J. Pérez-Ramirez, F. Kapteijn, J.A. Moulijn, Catalyst performance testing: bed dilution revisited, Chem. Eng. Sci. 57 (2002) 4921–4932.

[60] R.J. Berger, J. Pérez-Ramirez, F. Kapteijn, J.A. Moulijn, Catalyst performance testing: radial and axial dispersion related to dilution in fixed-bed laboratory reactors, Appl. Catal., A 227 (2002) 321–333.

[61] R.J. Berger, J. Pérez-Ramirez, F. Kapteijn, J.A. Moulijn, Catalyst performance testing: the influence of catalyst bed dilution on the conversion observed, Chem. Eng. J. 90 (2002) 173–183.

[62] F. Yoshida, D. Ramaswami, O.A. Hougen, Temperatures and partial pressures at the surfaces of catalyst particles, AIChE J. 8 (1962) 5–11.

[63] P.B. Weisz, C.D. Prater, Interpretation of measurements in experimental catalysis, Adv. Catal. 6 (1954) 143–196.

[64] J.B. Anderson, A criterion for isothermal behavior of a catalyst pellet, Chem. Eng. Sci. 18 (1963) 147–148.

[65] S. Ergun, Fluid flow through packed columns, Chem. Eng. Prog. 48 (1952) 89–94.

[66] P.G. Menon, J.C. De Deken, G.F. Froment, Formaldehyde as an intermediate in the steam reforming of methane, J. Catal. 95 (1985) 313–316.

[67] J. Wei, E. Iglesia, Isotopic and kinetic assessment of the mechanism of reactions of CH_4 with CO_2 or H_2O to form synthesis gas and carbon on nickel catalysts, J. Catal. 224 (2004) 370–383.

[68] L.H. Hosten, G.F. Froment, Parameter estimation in multiresponse models, Periodica Polytech., Chem. Eng. 19 (1975) 123–136.

[69] R. Rennhack, R. Heinisch, Kinetische untersuchung der reaktion zwischen methan und wasserdampf an nickel-oberflächen, Erdröl Kohle Erdgas Petrochem. 25 (1972) 22–29.

[70] J.C. De Deken, E.F. Devos, G.F. Froment, Steam reforming of natural gas: intrinsic kinetics, diffusional influences, and reactor design, ACS Symp. Series (1982) 181–197 Boston.

[71] B. Meyer, R. Köpsel, VEB Deutscher Verlag fur Grundstoff-Industrie, Leipzig, 1981.

[72] A. Obradovic, B. Likozar, J. Levec, Steam methane reforming over Ni-based pellet-type and $Pt/Ni/Al_2O_3$ structured plate-type catalyst: intrinsic kinetics study, Ind. Eng. Chem. Res. 52 (2013) 13597–13606.

[73] M. Boudart, D.E. Mears, M.A. Vannice, Congrès international Chimie Industrielle, Compte-Rendu 36, Industrie Chimique Belge 32 (I) (1967) 281.

[74] A. Wheeler, Reaction rates and selectivity in catalyst pores, Adv. Catal. 3 (1951) 249–327.

[75] C. Feng, W. Steward, Practical models for isothermal diffusion and flow of gases in porous solids, Ind. Eng. Chem. Fundam. 12 (1973) 143–147.

[76] F.J. Dumez, G.F. Froment, Dehydrogenation of 1-butene into butadiene. Kinetics, catalyst coking, and reactor design, Ind. Eng. Chem. Proc. Des. Dev. 15 (1976) 291–301.

[77] J. Beeckman, G.F. Froment, Deactivation of catalysts by coke formation in the presence of internal diffusional limitation, Ind. Eng. Chem. Fundam. 21 (1982) 243–250.

[78] S. Kolitcheff, E. Jolimaitre, A. Hugon, J. Verstraete, P.-L. Carrette, M. Tayakout-Fayolle, Tortuosity of mesoporous alumina catalyst supports : influence of the pore network organization, Microporous Mesoporous Mater. 248 (2017) 91–98.

[79] K.A. Akanni, J.W. Evans, I.S. Abramson, Effective transport coefficients in heterogeneous media, Chem. Eng. Sci. 42 (1987) 1945–1954.

[80] E.E. Petersen, Diffusion in a pore of varying cross section, AIChE J. 4 (1958) 343–345.

[81] H.L. Weissberg, Effective diffusion coefficient in porous media, J. Appl. Phys. 34 (1963) 2636–2639.

[82] M.M. Tomadakis, S.V. Sotirchos, Transport properties of random arrays of freely overlapping cylinders with various orientation distributions, J. Chem. Phys. 98 (1993) 616–626.